ARTICLE OPEN

Check for updates

Phase-field simulations of vortex chirality manipulation in ferroelectric thin films

Di Liu[1,2], Jing Wang[1,2], Hasnain Mehdi Jafri[1,2], Xueyun Wang [3], Xiaoming Shi[1,2], Deshan Liang [1,2], Chao Yang[1,2], Xingwang Cheng[1] and Houbing Huang [1,2✉]

The ferroelectric chiral vortex domains are highly desirable for the application of data storage devices with low-energy consumption and high-density integration. However, the controllable switching of vortex chirality remains a challenge in the current ferroelectric community. Utilizing phase-field simulations, we investigate the vortex domain evolution and chirality formation in $BiFeO_3$ thin films. By applying local surface charge or electric field, we demonstrate that the vorticity and the polarity can be manipulated by the initial bi-domain arrangement and the external field with different directions, respectively. By exchanging the domain arrangements, the opposite chirality can be obtained. Importantly, the topological vortex domain is retained after removing the external field. The vortex chirality can be switched reversibly with high reproducibility, which is beneficial to fatigue tolerance of the material in the operation. These results provide theoretical guidance for manipulating the vortex chirality in ferroelectric films.

npj Quantum Materials (2022)7:34 ; https://doi.org/10.1038/s41535-022-00444-8

INTRODUCTION

Chirality geometrically refers to the left-handed (LH) and right-handed (RH) phenomena[1], which allows materials with chiral properties to be widely used, such as polarization optics[2,3], sensors[4], and stereochemistry[5]. Recently, nanoscale textures in ferroelectric materials have also been demonstrated to exhibit chirality[6]. Chiral topological defects, such as magnetic skyrmions[7,8], polar vortices, and polar skyrmions[9–11], have been reported, and these phenomena have attracted tremendous interest in material science and condensed matter physics[12,13]. Moreover, the relative insensitivity of these small-sized textures to external disturbances host the ability for their use in highly robust next-generation information storage devices[14,15]. This, in turn, has increased interest in the controlled manipulation of vortex chirality in ferroelectric materials.

Here, $BiFeO_3$ (BFO) serves as one of the most prototypical ferroelectric materials[16]. It is shown that its inherent rhombohedral (R) structure determines the eight polarization orientations along the pseudo-cubic <111> directions, and the adjacent orientations also determine the diversity of its domain walls (DWs), including 180°, 109°, and 71° DWs[17]. Previously, the chirality at DWs has been speculated due to the depolarization field and stress/strain inhomogeneity[18,19]. In the experiment, DW chirality has been proved in triclinic ferroelectric crystals[20]. Then, chiral 71° and 109° DWs appear in BFO films owing to the different polarization rotation ways at DW, which is confirmed by using the reciprocal and real-space characterization techniques[21].

Theoretical works have reported that curled electric field (**E**) controls vortex chirality by switching toroid moment to form a new vortex in ferroelectric nanoparticles[22,23], and the interaction of polarization and strain promotes vortex formation. However, with the local radial **E** stimulation, ferroelectric vortex pairs were created or annihilated in films by selecting the appropriate polarization location[24–26], and characteristic shaped or graded composition[27–29]. In addition, the mechanical field was proven to

control vortex morphology[29–31]. As for the interface strain, it also promotes polarization rotation to form a pair of opposite vortices[32]. Among them, the influence of flexoelectricity on polarization switching and DW formation has been extensively explored[18,33,34]. These results indicate that vortex evolution is sensitive to flexoelectricity[35–37], and the flexoelectric coupling coefficients can be quantified by phase-field methods, where the vortex morphology is reflected[38].

Based on the phase-field simulation, this work focuses on the formation mechanism and controllable manipulation of chiral vortices in a single domain and bi-domain in BFO thin films under local surface charge or electric field. The simulation results demonstrate that the bi-domain arrangements determine the in-plane vorticity. The chirality is related to the initial bi-domain arrangements. Importantly, the chirality is reversibly switched by applying alternating surface charge or electric field. The vortex chirality remains unchanged after removing the external field. This study advances our understanding of vortex domain evolution and chirality manipulation in ferroelectric thin films.

RESULTS AND DISCUSSION

The emergent chirality in the vortex

The schematics of four types of chirality defined according to the out-of-plane polarity and in-plane vorticity of the polarization vectors (**P**)[39–41] are shown in Fig. 1. The out-of-plane polarity points downward, that is, $P_z < 0$ (marked as a black cross), which is defined as OP = −1. When the out-of-plane polarity is upward, that is, $P_z > 0$ (marked as double black circles), then is defined as OP = +1. In addition, counterclockwise vorticity is CCW = −1 and clockwise vorticity is CW = +1, and the black arrows indicate the projection of the polarization in the x-y plane. The chirality is then defined as the product of the polarity and the vorticity. Accordingly, LH chirality is defined as LH = 1, which includes a CCW (−1) vorticity with downward (−1) polarity, and a CW (+1)

[1]School of Materials Science & Engineering, Beijing Institute of Technology, Beijing 100081, China. [2]Advanced Research Institute of Multidisciplinary Science, Beijing Institute of Technology, Beijing 100081, China. [3]School of Aerospace Engineering, Beijing Institute of Technology, Beijing 100081, China. ✉email: hbhuang@bit.edu.cn
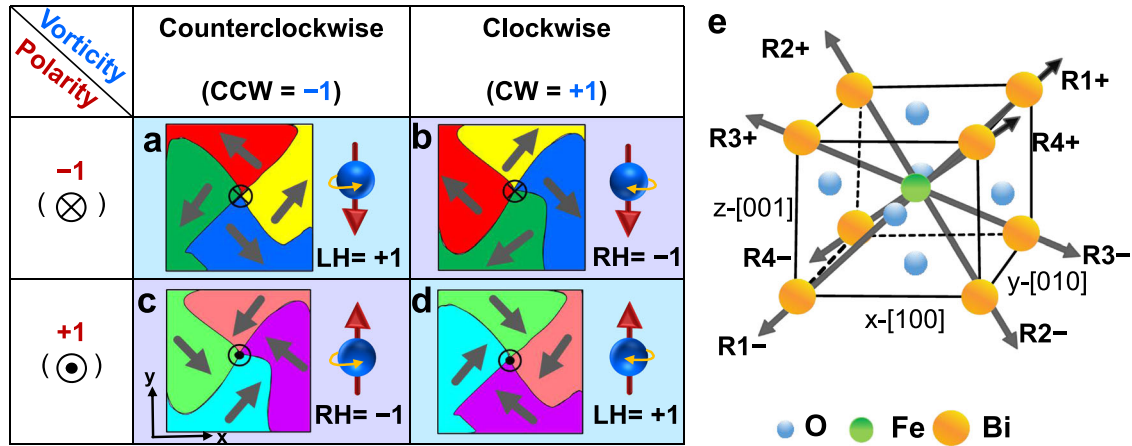
Fig. 1 Schematics of the four types of ferroelectric vortices with LH (+1) and RH (−1) chirality. LH vortex based on either **a** −1 vorticity and −1 polarity or **d** +1 vorticity and +1 polarity; RH vortex based on either **b** +1 vorticity and −1 polarity or **c** −1 vorticity and +1 polarity. The black arrows denote the in-plane polarization direction, and the cross and dot denote the downward or upward out-of-plane polarization direction, respectively. **e** The eight polarization variants along with the <111> BFO crystal orientation.

vorticity with upward (+1) polarity, as shown in Fig. 1a, d, respectively. Similarly, RH chirality is defined as RH = −1, which includes a CW (+1) vorticity with downward polarity (−1), and a CCW (−1) vorticity with upward polarity (+1), as shown in Fig. 1b, c, respectively. Figure 1e is a schematic of the eight polarization variants in R BFO. According to the symmetry, there are four upward (R1+, R2+, R3+, and R4+) and four downward (R1−, R2−, R3−, and R4−) polarization variants, respectively.

The vortex chirality in the single domain

First, we apply positive/negative surface charge on the top surface of the 10 nm BFO thin film with an initial single domain, and the vortex can be generated as shown in Fig. 2a, b. The results of the other four initial single domains (R1−, R2−, R3−, and R4−) are shown in Supplementary Fig. 1. Figure 2c shows that nine positive surface charge regions are applied on BFO thin film with an initial R1+ domain. Interestingly, the vortex chirality is random with the initial single domain due to the degenerate energy state of polarization. Then, it should be noticed that the downward polarization switching appears in the local region with applied surface charge, whereas the domains with upward P_z appear around the vortex. Here, the applied local positive surface charge is equivalent to a downward built-in electric field. The positive surface charge favors the negative polarization bound charge, and the in-plane domains with outward center-divergent polarization directions are formed[13,25]. In addition, the out-of-plane polarization points downward due to the negative built-in electric field. Then, topological domains form with polarization orientations along with the $[\overline{1}1\overline{1}]$, $[1\overline{1}\overline{1}]$, $[11\overline{1}]$, and $[\overline{1}\overline{1}\overline{1}]$. In domain evolution, the four-quadrant topological domain with the straight DWs in a high-energy state evolves into the vortex with curved DWs.

Although we cannot controllably manipulate the vortex chirality in a single domain, the discrepancy in polarization switching of different initial domains can promote us to recognize the formation mechanism of vortex domains. The percentages of four negative R domains induced in the single domain are shown in Fig. 2f. The results show that the percentage of R domains formed by 71° polarization switching (e.g., R1+ → R3−) is larger than that formed by 109° (e.g., R1+ →R2−, R4−) and 180° (e.g., R1+ →R1−) switching. Here, the height of the energy barrier determines the difficulty of the path of polarization switching[42].

Then, we further explore the influence of surface charge density (σ_{surf}) on the domain evolution, as shown in Fig. 3. The domain structures under applied different positive σ_{surf} are shown in Fig. 3a, and the corresponding energy densities evolution is

shown in Fig. 3c. R1+ single variants are initial states and the R domains with downward out-of-plane polarization ($P_z < 0$) are induced by applying positive charges. When the σ_{surf} is 0.08 Cm^{-2}, R3− domain is dominant. As the σ_{surf} continues to increase, the R1− domain region gradually increases. When the σ_{surf} is 0.8 Cm^{-2}, a vortex with evenly distributed 4 R domains forms, as shown in Fig. 3a. The square-shaped local positive surface charge region is applied on the top surface, and the downward domain switching occurs in the charged region. Then, the surrounding domains ($P_z > 0$) are formed to minimize the stray electric field. The polarization switching mechanism affects the R domain ratio in a single vortex, and 71° ferroelastic switching is the easiest. The surface charge densities determine the domain switching path, which in turn affects the vortex domain morphology. At the same time, the vortex core moves toward the center of the film with the σ^*_{surf} increases, as shown in Fig. 3b.

The corresponding energy density (f) evolution is shown in Fig. 3c, where the decrease in $f_{electric}$ is due to the contribution of the built-in electric field caused by the increase in surface charge. The expression of f_{Landau} (Eq. 3) is closely related to polarization, where an increase in surface charge induces more polarization switching and leads to the increase of DW density, thereby increasing the Landau energy. When 71° DW converges to form a vortex, the vortex core exhibits continuous polarization rotation. To minimize the free energy and electrostatic energy of the system, the domain configurations transform to a curved DW in a metastable state, as shown in Supplementary Fig. 2.

The vortex chirality manipulation in bi-domain

The DW is the key to breaking the radial symmetry of the external field, which is conducive to the formation of more interesting topological vortex patterns[24,43]. A bi-domain arrangements with initial R3+|R3− polarization states are separated by 180° DW oriented along the y axis, and LH chiral vortex with CCW rotation can be obtained in Fig. 4a, as indicated by the polarization vector plot. Then, by reversing the initial bi-domain arrangement from R3+|R3− to R3−|R3+, an RH vortex with CW rotation is induced as shown in Fig. 4b. We also consider bi-domain arrangements with initial R3+|R2− states separated by a 109° DW oriented along the y axis, as shown in Fig. 4c, and the reversed domain arrangement with initial R2−|R3+ states is shown in Fig. 4d. The LH chiral vortex domain with CCW rotation can be obtained, and the polarization projection in the x–y plane is shown in vector plots, respectively. The polarization orientation of the initial bi-domain determines vortex chirality. In other
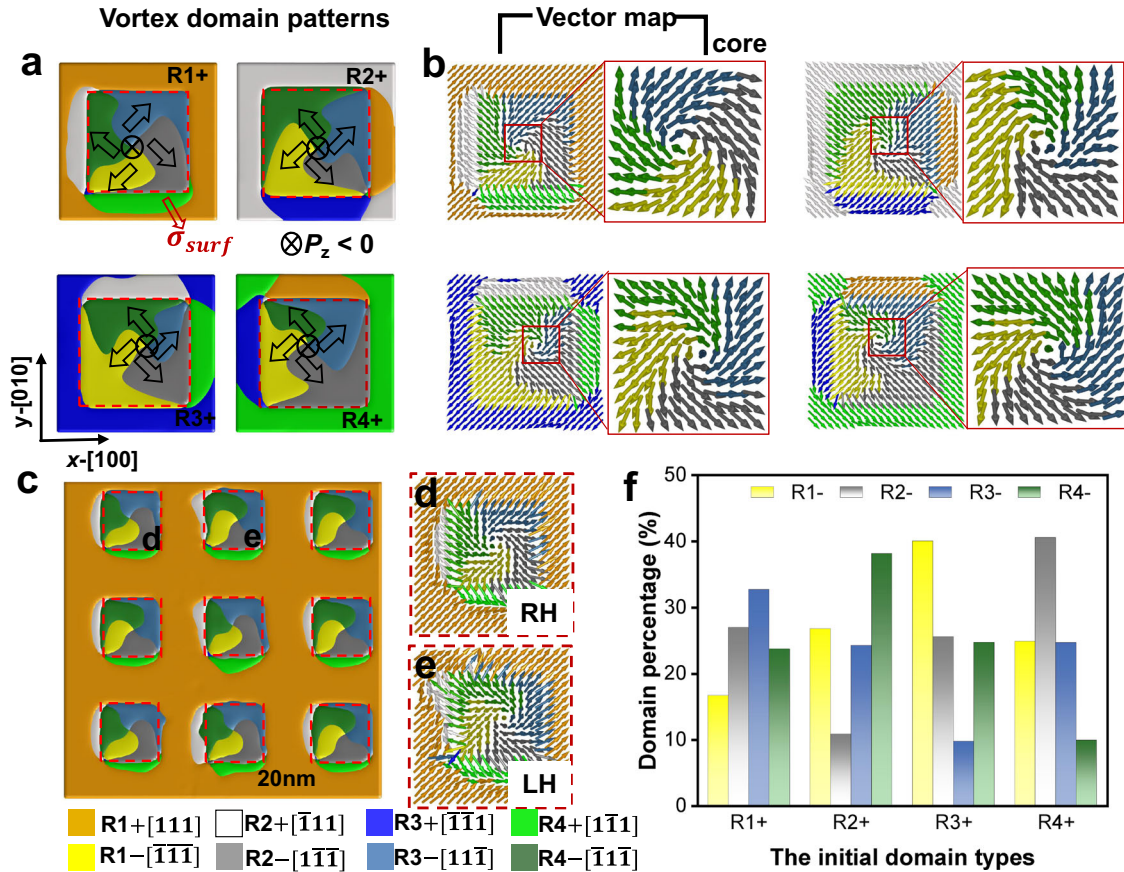
Fig. 2 Chiral polar vortices induced by applying a local square-shaped positive surface charge. a The vortex domain patterns in four initial upward single domains (R1+, R2+, R3+, and R4+, respectively). **b** The projection of the polarization vector. **c** Nine vortices are induced by applying nine charge regions on large-scale BFO thin film with an initial R1+ domain. The polarization vector distribution of RH vortex in **d** and LH vortex in **e**. **f** The final domain percentages in a vortex indued in four initial domains. Yellow, gray, steel-blue, and steel-green regions represent domains with polarization along with R1−($[\bar{1}\bar{1}1]$), R2−($[1\bar{1}\bar{1}]$), R3− ($[11\bar{1}]$), and R4− ($[\bar{1}1\bar{1}]$) directions, respectively.

words, the polarization components along the DW in the bi-domain are opposite, which have the opposite vortex chirality, and vice versa. Through reversing the domain arrangements, the vortex chirality is reversed. More information about 180°, 109°, and 71° DWs with the bi-domain combination are summarized in Supplementary Figs. 3–5, respectively. The results of 180° DW indicate that opposite vortex chirality can be obtained by swapping the initial bi-domain arrangement. The results of 109° and 71° DW demonstrate that deterministic switchable vortex chirality can be obtained by converting the initial bi-domain arrangement into specific bi-domain combinations.

Here, the inherent DW chirality makes contributions to the charge-induced vortex chirality. In R3+|R3−, the polarization components (P_y) in two adjacent domains have opposite directions and show CCW vorticity seen from the right to the left so that the charge-induced vortex is CCW. In R3−|R3+, P_y shows CW vorticity so that the charge induces a CW vortex. The two P_y are in the same direction in Fig. 4b, d, so the two vortices have similar rotation directions. However, the charged 109° DW (R3+|R2−) are mechanically incompatible, but the final states of these DWs are stable in the modeling due to enough screening charges in short-circuit electrostatic boundary conditions. To understand the effect of mechanical compatibility of initial DW on vortex chirality, the charge-induced chiral vortices are obtained in neutral and mechanical permissible 109° DWs (R1+|R2− and R3−|R4+)[44,45], respectively, as shown in Supplementary Fig. 6. In R1+|R2− and R3−|R4+, the opposite vortex chirality is obtained after exchanging the bi-domain arrangements owing to the

opposite P_y in adjacent domains. The inherent P_y rotation direction determines the vortex chirality, these results further confirm the above discussions.

To study the influence of DW orientation on the vortex chirality, we switch the DW orientation along the x axis, as shown in Fig. 4e–h. Opposite chirality is obtained by reversing the bi-domain arrangement from R3+/R3− to R3−/R3+, respectively, as shown in Fig. 4e, f. Similarly, reversing the initial R3+/R2− to R2−/R3+, RH and LH vortices are obtained, respectively, as shown in Fig. 4g, h. Similarly, a pair of controllable chiral vortex domains, including polarity and vorticity type, can also be successfully achieved in the initial tri-domain combination, as shown in Supplementary Fig. 7.

The chirality formation is closely related to the initial bi-domain arrangements, the detailed evolution is shown in Supplementary Fig. 8. As we know, four R domains positions are fixed due to the crystal orientation in R-BFO films[46,47]. In R3+|R3—bi-domains [Supplementary Fig. 8a], at left-panel, R1− domain is larger than R4−, by 71° and 109° switching. On the right panel, positive σ_{surf} determines the larger R3− domain. Then, the straight four R domains gradually evolve into an LH vortex. However, an RH vortex is shown in R3−|R3+ bi-domains [Supplementary Fig. 8b], at left-panel, the switched largest domain area is R3−. On the right panel, the largest switched domain area is R1− through 71° switching. To minimize the system energy, the small R domains merge into the same large domains to form a chiral vortex. Therefore, the initial bi-domain arrangement determines the largest R domain position, which in turn determines the final
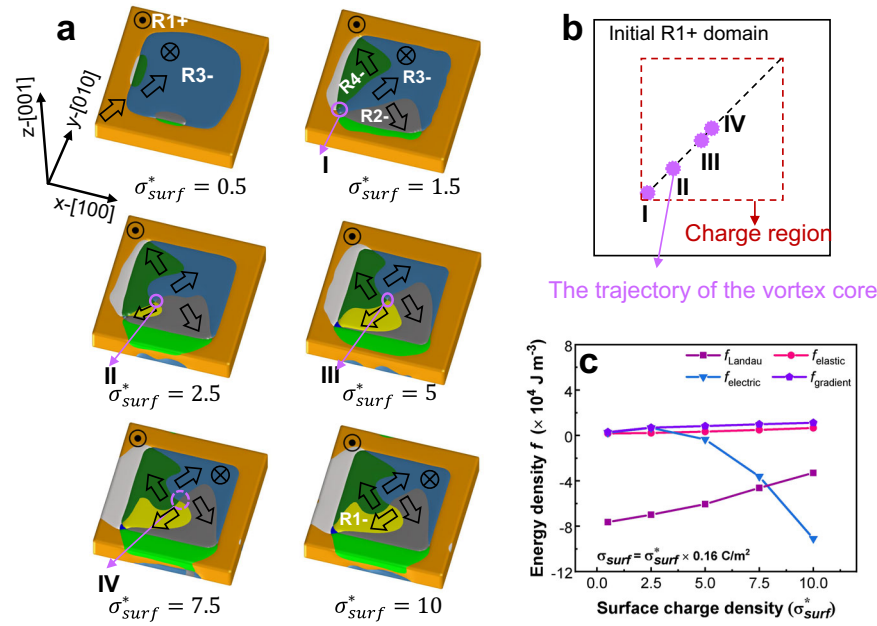
Fig. 3 The domain evolution with different positive surface charge densities (σ_{surf}). a Domain evolution with different σ_{surf}. σ^*_{surf} is normalized value ($\sigma_{surf} = \sigma^*_{surf} \times 0.16\,C/m^2$). **b** The trajectory of the vortex core movement. **c** The energy density distribution vs positive surface charge density.
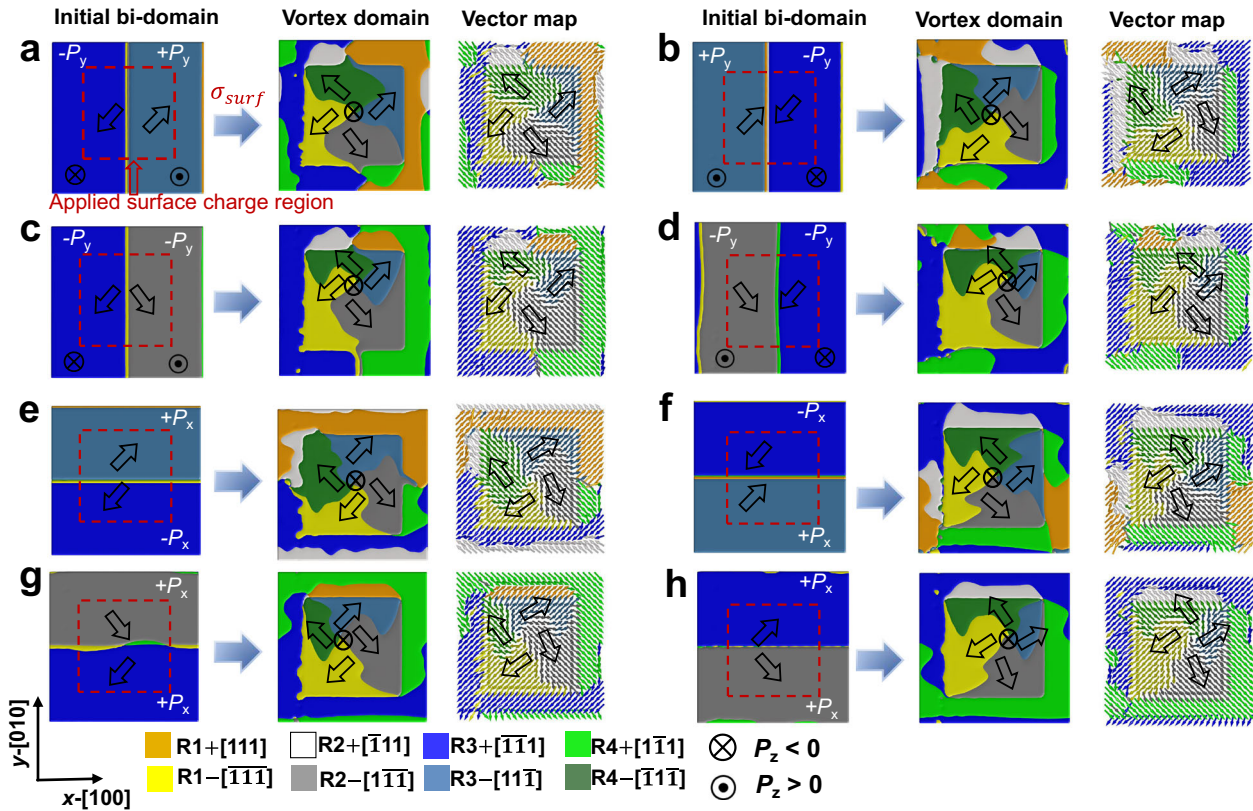

Fig. 4 The manipulation of vortex chirality by bi-domain arrangements. The bi-domain arrangements are separated by 180° and 109° DWs oriented along the y axis: **a** Initial R3+|R3− polarization arrangement and LH chiral vortex. **b** Initial R3−|R3+ polarization arrangement and RH chiral vortex. **c** Initial R3+|R2− polarization arrangement and LH chiral vortex. **d** Initial R2−|R3+ polarization arrangement and LH vortex. The bi-domain arrangements are separated by 180° and 109° DWs oriented along the x axis. **e** Initial R3+/R3− polarization arrangement and RH vortex. **f** Initial R3−/R3+ polarization arrangement and LH vortex. **g** Initial R3+/R2− polarization arrangement and RH vortex. **h** Initial R2−/R3+ polarization arrangement and LH vortex.
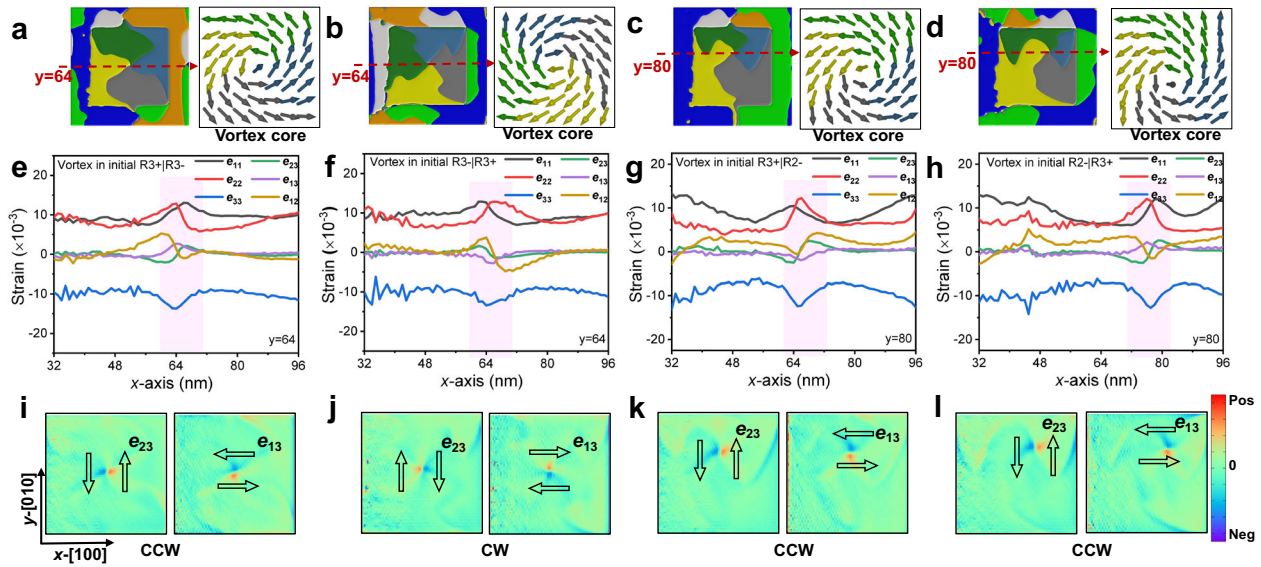
Fig. 5   The elastic strain (e_{11}, e_{22}, e_{33}, e_{23}, e_{13}, e_{12}) distribution in the vortex domain. a–d The vortex structure and the enlarged core polarization vector map are viewed in x–y cross-section. **e–f** The strain distribution in chiral vortex along the red dashed line in **a–d**, respectively. **i–l** The distribution of shear strain (e_{23}, e_{13}) in the chiral vortex, respectively. The arrows indicate the shear strain direction.

vorticity. The charge-induced vortex chirality is closely related to the initial bi-domain.

Although the successful application of surface charge-induced polarization switching in the electrochemistry[48,49], the common path to achieve domain switching is the electric field or the electric bias in the experiments[25,46,50]. Therefore, the local radial electric fields created by applying square-shaped surface potential are studied on the bi-domain BFO films with 180° DWs, the surface potential distributions are shown in Supplementary Fig. 9. The results are consistent with the case of surface charge, a specific vortex chirality can be obtained by applying a local external electric field in the ordered initial bi-domain.

The strain distribution in the chiral vortex

In ferroelectric materials, there is an electrostrictive coupling effect between ferroelectric polarization and intrinsic strain (ε_{ij}^0). Therefore, the elastic strain (e_{ij}) distribution can reflect the ferroelectric polarization distribution to a certain extent (Seen in Eq. (7)). We calculate elastic strain (e_{ij}) in chiral vortex induced by initial R3+ |R3−, R3−|R3+, R3+|R2− and R2−|R3+ bi-domain, respectively. Figure 5e–h shows elastic strain distributions along the corresponding red dashed line of Fig. 5a–d, respectively. For all the strain distributions, the axial strains e_{11}, e_{22}, and e_{33} change significantly near the vortex core, e_{11} and e_{22} are tensile strains and e_{33} is compressive. By comparing Fig. 5e, f, the shear strains e_{23} and e_{13} show different evolution behavior. Therefore, we plot the shear strain (e_{23} and e_{13}) distribution along the 2D x-y plane in Fig. 5i–l. The e_{23} and e_{13} have maximum and minimum values with the opposite signs on both sides of the core, and we add the arrows to indicate the direction of e_{23} and e_{13}. In Fig. 5i, j, both e_{23} and e_{13} all have opposite directions, so the vortices show CCW rotation and CW rotation, respectively. Similarly, in Fig. 5k, l, e_{23} and e_{13} have the same direction on both sides of the core, so the vortices are all CCW rotation. The shear strains (e_{23} and e_{13}) have closely related to the vortex vorticity in the core.

The external field manipulation of vortex chirality

To explore the influence of the flexoelectric effect, the bi-domain combinations of R3+|R3− of 180° DW are selected as the initial states, as shown in Supplementary Fig. 10. The vortex chirality remains LH by considering the flexoelectric effect. Then, the strain

gradient of the in-plane elastic strain (e_{11}, e_{22}) and out-of-plane elastic strain (e_{33}) along the z axis slightly increase due to the flexoelectric coupling coefficients. Here, the flexoelectric effect contributes to the morphology of the vortex domain but does not change the chirality of the ferroelectric vortex.

To further achieve chirality switching, we demonstrate the reversible control of vortex chirality by alternating external fields. The schematics of alternate application of σ_{surf} and E are shown in Fig. 6a, b, respectively. The reversible chirality of the vortex domain can be obtained by applying $\pm\sigma_{surf}$ and $\pm E$, as shown in Fig. 6c, d, respectively. These results demonstrate that the out-of-plane polarity changes with the sign of the external field in the vortex, while the vorticity is unchanged. Here, the width of the charge region (W_c) is 80 nm in Fig. 6, The stray electric field induces the outer domain with opposite P_z direction. The adjacent inner and outer domains are 71° out-of-plane polarization orientation, which decreases the large out-of-plane depolarization field to protect the inner vortex domain stability. Then, to study the vortex stability, the topological chiral vortices are relaxed after we remove the surface charge. The morphology of the vortex domain shrinks slightly, while the chirality of the vortex remains stable, the surrounding domains remain stable and the 71° out-of-plane orientation relationship is still in the inner vortex domain and surrounding outer domains, as shown in Supplementary Fig. 11. To understand the effect of the surface charge region size on the stability of the chiral vortex, we apply two widths of the charge region (W_c = 40 nm, 60 nm) on the 180° DWs, as shown in Supplementary Fig. 12. When we remove the surface charge, the chiral vortex in a small charge region is unstable and the vortex merges with the surrounding domains and becomes a striped domain. Here, the outer large domains make the inner small vortex merge and disappear. Therefore, the vortex stability is closely related to the large charge region size in BFO films.

In short, the ferroelectric vortices can be induced in initial single and bi-domain regions under local surface charge and electric field stimulation. In a single domain, the initial domains determine the percentage and morphology of the vortex domain, the vortex formation requires sufficient surface charge density. As the charge density increases, the vortex core moves to the center. Our results show that vortex chirality is controllably manipulated by selecting the initial bi-domain arrangement with typical DWs. The inherent DW chirality determines the charge-induced vortex chirality.
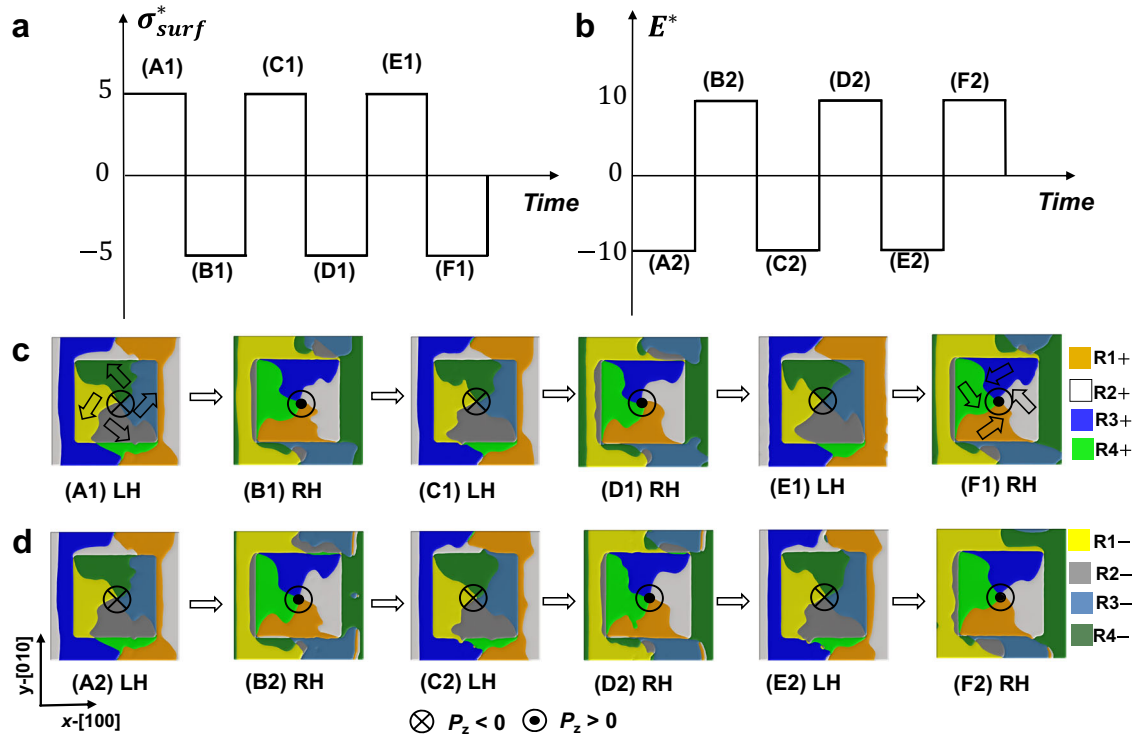
Fig. 6 Reversible control of vortex chirality via alternating external stimuli. a Schematic of surface charge application. **b** Schematic of electric field application. **c** Reversible vortex chirality evolution under the stimuli presented in (**a**). **d** Reversible vortex chirality evolution under the stimuli presented in (**b**). The * is a normalized value, $E^* = E \times 0.192$ MV/cm.

In other words, if the initial bi-domain polarization component's direction along the DW are opposite, the opposite vortex chirality can be obtained. The sign of the external field determines the vortex polarity, thus successfully regulating chirality. After we remove the external field, the vortices are stable only in the region with previously applied large enough charge density. These results provide a basis for understanding the chirality manipulation and vortex evolution in ferroelectric thin films.

METHODS

In the phase-field simulation, the ferroelectric polarization evolutions are described by the time-dependent Ginzburg–Landau equation[51–53]:

$$\frac{\partial P_i(\mathbf{r}, t)}{\partial t} = -L \frac{\delta F}{\delta P_i(\mathbf{r}, t)}, \, (i = 1, 2, 3) \tag{1}$$

where P_i is the component of the polarization along with the [1 0 0] (x axis; $i = 1$), [0 1 0] (y axis; $i = 2$), and [0 0 1] (z axis; $i = 3$) crystal orientations in Cartesian coordinates, $\mathbf{r}$ and t are the spatial position vector and the simulation time, respectively, L is related to DW mobility, and f_{total} is the total free energy density in the thin film, which is determined by the Landau free energy density (f_{Landau}), gradient energy density ($f_{gradient}$), electrostatic energy density ($f_{electric}$), and elastic energy density ($f_{elastic}$), and flexoelectric energy density (f_{flexo}):

$$f_{total} = f_{Landau} + f_{gradient} + f_{electric} + f_{elastic} + f_{flexo} \tag{2}$$

We define f_{Landau} as the following sixth-order polynomial,

$$\begin{aligned}
f_{Landau} &= a_1(P_1^2 + P_2^2 + P_3^2) + a_{11}(P_1^4 + P_2^4 + P_3^4) + a_{12}(P_1^2 P_2^2 + P_2^2 P_3^2 + P_1^2 P_3^2) \\
&\quad + a_{111}(P_1^6 + P_2^6 + P_3^6) + a_{112}[P_1^2(P_2^2 + P_3^2) + P_2^2(P_3^2 + P_1^2) \\
&\quad + P_3^2(P_1^2 + P_2^2)] + a_{123}P_1^2 P_2^2 P_3^2
\end{aligned} \tag{3}$$

where a_1, a_{11}, a_{12}, a_{111}, a_{112}, and a_{123} are the dielectric stiffness and high order stiffness coefficients[54]. According to the Curie–Wiess law, a_1 depends on the temperature, and it can be defined as $a_1 = (T - T_0)/(2\varepsilon_0 C_0)$ where T is

temperature, T_0 is the Curie temperature, the vacuum dielectric constant is $\varepsilon_0 = 8.85 \times 10^{-12}$ Fm^{-1}, and C_0 is the Curie constant.

We define $f_{gradient}$ in terms of polarization gradients as follows:

$$f_{gradient} = \frac{1}{2} G_{ijkl} P_{i,j} P_{k,l}, \, (i, j, k, l = 1, 2, 3) \tag{4}$$

where G_{ijkl} is the gradient energy coefficient tensor. Here, G_{ijkl} can be simplified as G_{11}, G_{12}, G_{44}, and G_{44}' to obtain the following: $f_{gradient} = \frac{1}{2}G_{11}(P_{1,1}^2 + P_{2,2}^2 + P_{3,3}^2) + G_{12}(P_{1,1}P_{2,2} + P_{3,3}P_{2,2} + P_{3,3}P_{1,1}) + \frac{1}{2}G_{44}[(P_{1,2} + P_{2,1})^2 + (P_{2,3} + P_{3,2})^2 + (P_{1,3} + P_{3,1})^2] + \frac{1}{2}G_{44}'[(P_{1,2} - P_{2,1})^2 + (P_{2,3} - P_{3,2})^2 + (P_{1,3} - P_{3,1})^2]$.

The flexoelectric energy density f_{flexo} can be expressed as

$$f_{flexo} = \frac{f_{ijkl}}{2}\left(e_{ij}\frac{\partial P_k}{\partial x_l} - P_k \frac{e_{ij}}{\partial x_l}\right), \, (i, j, k, l = 1, 2, 3) \tag{5}$$

where f_{ijkl} represents flexoelectric coupling coefficients and e_{ij} is elastic strain. For cubic symmetry, f_{ijkl} can be simplified as f_{11}, f_{22}, f_{44} in Voigt's notation. Here, the flexoelectric coupling coefficients are set as: $f_{11} = 2.5$ V, $f_{22} = 2.5$ V, $f_{44} = 0.05$ V, based on reasonable estimation[55]. Then, the driving force from the flexoelectric effect (E_i^{flexo}) can be calculated as follows:

$$\frac{\delta f_{flexo}}{\delta P_1} = -f_{11}\frac{\partial e_{11}}{\partial x_1} - f_{12}\left(\frac{\partial e_{22}}{\partial x_1} + \frac{\partial e_{33}}{\partial x_1}\right) - f_{44}\left(\frac{\partial e_{13}}{\partial x_3} + \frac{\partial e_{12}}{\partial x_2}\right) = -E_1^{flexo}$$

$$\frac{\delta f_{flexo}}{\delta P_2} = -f_{11}\frac{\partial e_{22}}{\partial x_2} - f_{12}\left(\frac{\partial e_{33}}{\partial x_2} + \frac{\partial e_{11}}{\partial x_2}\right) - f_{44}\left(\frac{\partial e_{12}}{\partial x_1} + \frac{\partial e_{23}}{\partial x_3}\right) = -E_2^{flexo} \tag{6}$$

$$\frac{\delta f_{flexo}}{\delta P_3} = -f_{11}\frac{\partial e_{33}}{\partial x_3} - f_{12}\left(\frac{\partial e_{11}}{\partial x_3} + \frac{\partial e_{22}}{\partial x_3}\right) - f_{44}\left(\frac{\partial e_{23}}{\partial x_2} + \frac{\partial e_{13}}{\partial x_1}\right) = -E_3^{flexo}$$

The elastic energy density $f_{elastic}$ can be written as

$$f_{elastic} = \frac{1}{2}c_{ijkl}e_{ij}e_{kl} = \frac{1}{2}c_{ijkl}(\varepsilon_{ij} - \varepsilon_{ij}^0)(\varepsilon_{kl} - \varepsilon_{kl}^0), \, (i, j, k, l = 1, 2, 3) \tag{7}$$

where c_{ijkl}, e_{ij}, ε_{ij}, and ε_{ij}^0 is the elastic stiffness tensor, elastic strain, total strain, and eigenstrain of BFO films, respectively. The eigenstrain is $\varepsilon_{ij}^0 = Q_{ijkl}P_k P_l$, Q_{ijkl} is an electrostrictive coefficient tensor and can be marked as Q_{11}, Q_{22}, and Q_{44} due to the symmetry. Here, there are three elastic constants of c_{11}, c_{12}, and c_{44} in Voigt's notation for a cubic symmetry.

Table 1. The material coefficients of $BiFeO_3$ are used in phase-field simulations.

Coefficients	Value	Coefficients	Value
a_1 ($\times 10^8$ C^{-2}m^{2}N)	-3.73	c_{11} (Nm^{-2})	2.280×10^{11}
a_{11} ($\times 10^8$ C^{-4}m^{6}N)	2.29	c_{12} (Nm^{-2})	1.250×10^{11}
a_{12} ($\times 10^8$ C^{-4}m^{6}N)	3.06	c_{44} (Nm^{-2})	6.500×10^{10}
a_{111} ($\times 10^7$ C^{-6}m^{10}N)	5.99	Q_{11} (C^{-2}m^4)	0.032
a_{112} ($\times 10^5$ C^{-6}m^{10}N)	-3.34	Q_{12} (C^{-2}m^4)	-0.016
a_{123} ($\times 10^8$ C^{-6}m^{10}N)	-1.78	Q_{44} (C^{-1}m^4)	0.02
G_{11} (C^{-2}m^{4}N)	0.6	T (K)	300
G_{12} (C^{-2}m^{4}N)	0	$k_{11} = k_{22} = k_{33}$	45
G_{44} (C^{-2}m^{4}N)	0.3	P_0 (Cm^{-2})	0.52
f_{11} (V)	2.5	f_{22} (V)	2.5
f_{44} (V)	0.05	$\varepsilon_{xx} = \varepsilon_{yy}$	0

The top surface of films is stress-free and the bottom is constrained by the substrate. In the bottom surface of the film, the equal biaxial misfit strain is considered along the x and y directions. The elastic stress is $\sigma_{ij} = c_{ijkl}e_{ij} = c_{ijkl}(\varepsilon_{ij} - \varepsilon_{ij}^0)$, and the mechanical equilibrium equation is $\sigma_{ij,j} = \frac{\partial \sigma_{ij}}{\partial x_j} = 0$ $(i, j = 1 - 3)$. Here, on the top surface of the film $\sigma_{i3}|_{x3=nf} = 0$.

The electrostatic energy density f_{electric} can be written as

$$f_{\text{electric}} = -P_i E_i - \frac{1}{2}\varepsilon_0 k_{ij} E_i E_j \qquad (8)$$

where ε_0 is the vacuum dielectric constant, and k_{ij} represents the background dielectric constants[56], and here the isotropic k_{ij} is taken as $k_{11} = k_{22} = k_{33} = 45$, which is consistent with the adopted value of the previous references[57]. Electrostatic energy comes from two contributions, one comes from spontaneous polarization, and the other comes from energy storage in vacuum space. The contributions of polarization come from the ionic displacements and background dielectric constants. $E_i = -\nabla_i \varphi = -\frac{\partial \varphi}{\partial x_i}$ is an electrostatic field, φ is electric potential. The short-circuit boundary conditions are applied to solve the electrostatic equilibrium equation, which avoids the depolarization effect and bound charge screening effect. Then, the surface charge density (σ_{surf}) is applied on the top surface of thin films and the free charge density has the following boundary condition: $\rho|_{z=nf} = \sigma_{\text{surf}}$, and $\rho = 0$ in the thin film. Assuming that the σ_{surf} is that the charge occupies each grid point, $\sigma_{\text{surf}} = \sigma_{\text{surf}}^* \times$ electrons$/S_{\text{grid\_area}}$, one grid size is $S_{\text{grid\_area}} = 1.0 \times 10^{-18}$ m^2 and one electron is equal to 1.6×10^{-19} C.

Accordingly, the electrostatic potential $\varphi(\mathbf{r})$ at the thin film surface can be solved by electrostatic equilibrium (Poisson) equation[58],

$$\Delta \varphi|_{z=nf} = \frac{\nabla \cdot P_i - \rho|_{z=nf}}{\varepsilon_0 k_{ii}} \ (i = 1, 2, 3) \qquad (9)$$

where n_f is the thickness of the thin film. The details of boundary conditions can be seen in ref. [33].

In the simulations, the three-dimensional sizes of the simulated systems are $64\Delta x \times 64\Delta x \times 16\Delta x$ for a single domain, where $\Delta x = 1$ nm, and $128\Delta x \times 128\Delta x \times 16\Delta x$ for bi-domains, and $240\Delta x \times 240\Delta x \times 16\Delta x$ for tri-domain. In addition, the thickness of BFO film is 10 nm ($n_f = 10\Delta x$), and the material coefficients of BFO are listed in Table 1.

DATA AVAILABILITY

The data that support the findings of this study are available from the corresponding author upon reasonable request.

REFERENCES

1. Tanaka, Y. et al. Right handed or left handed? forbidden x-ray diffraction reveals chirality. *Phys. Rev. Lett.* **100**, 145502 (2008).
2. Gansel, J. K. et al. Gold helix photonic metamaterial as broadband circular polarizer. *Science* **325**, 1513 (2009).
3. Zhang, S. et al. Photoinduced handedness switching in terahertz chiral meta-molecules. *Nat. Commun.* **3**, 942 (2012).
4. Hendry, E. et al. Ultrasensitive detection and characterization of biomolecules using superchiral fields. *Nat. Nanotechnol.* **5**, 783–787 (2010).
5. Saito, K. et al. Chiral plasmonic nanostructures fabricated by circularly polarized light. *Nano Lett.* **18**, 3209–3212 (2018).
6. Shafer, P. et al. Emergent chirality in the electric polarization texture of titanate superlattices. *PNAS* **115**, 915 (2018).
7. Boulle, O. et al. Room-temperature chiral magnetic skyrmions in ultrathin magnetic nanostructures. *Nat. Nanotechnol.* **11**, 449–454 (2016).
8. Hu, J.-M. et al. Stability and dynamics of skyrmions in ultrathin magnetic nanodisks under strain. *Acta Mater.* **183**, 145–154 (2020).
9. Lin, S.-Z. et al. Topological defects as relics of emergent continuous symmetry and Higgs condensation of disorder in ferroelectrics. *Nat. Phys.* **10**, 970–977 (2014).
10. Tang, Y. L. et al. Observation of a periodic array of flux-closure quadrants in strained ferroelectric PbTiO₃ films. *Science* **348**, 547 (2015).
11. Das, S. et al. Observation of room-temperature polar skyrmions. *Nature* **568**, 368–372 (2019).
12. Damodaran, A. et al. Phase coexistence and electric-field control of toroidal order in oxide superlattices. *Nat. Mater.* **16**, 1003–1009 (2017).
13. Yang, W. et al. Quasi-one-dimensional metallic conduction channels in exotic ferroelectric topological defects. *Nat. Commun.* **12**, 1306 (2021).
14. Naumov, I. I. et al. Unusual phase transitions in ferroelectric nanodisks and nanorods. *Nature* **432**, 737–740 (2004).
15. Eshita, T. et al. Development of highly reliable ferroelectric random access memory and its internet of things applications. **57**, 11UA01 (2018).
16. Dong, S. et al. Multiferroic materials and magnetoelectric physics: symmetry, entanglement, excitation, and topology. *Adv. Phys.* **64**, 519–626 (2015).
17. Zhao, T. et al. Electrical control of antiferromagnetic domains in multiferroic BiFeO₃ films at room temperature. *Nat. Mater.* **5**, 823–829 (2006).
18. Yudin, P. V. et al. Bichiral structure of ferroelectric domain walls driven by flexoelectricity. *Phys. Rev. B* **86**, 134102 (2012).
19. Gu, Y. et al. Flexoelectricity and ferroelectric domain wall structures: phase-field modeling and DFT calculations. *Phys. Rev. B* **89**, 174111 (2014).
20. Cherifi-Hertel, S. et al. Non-Ising and chiral ferroelectric domain walls revealed by nonlinear optical microscopy. *Nat. Commun.* **8**, 15768 (2017).
21. Chauleau, J.-Y. et al. Electric and antiferromagnetic chiral textures at multiferroic domain walls. *Nat. Mater.* **19**, 1–5 (2020).
22. Naumov, I. et al. Cooperative response of Pb(ZrTi)O₃ nanoparticles to curled electric fields. *Phys. Rev. Lett.* **101**, 197601 (2008).
23. Wang, J. Intrinsic switching of polarization vortex in ferroelectric nanotubes. *Phys. Rev. B* **80**, 012101 (2009).
24. Vasudevan, R. K. et al. Exploring topological defects in epitaxial BiFeO₃ thin films. *ACS Nano.* **5**, 879–887 (2011).
25. Li, Y. et al. Rewritable ferroelectric vortex pairs in BiFeO₃. *npj Quant. Mater.* **2**, 43 (2017).
26. Kim, J. et al. Artificial creation and separation of a single vortex–antivortex pair in a ferroelectric flatland. *npj Quant. Mater.* **4**, 29 (2019).
27. Van Lich, L. et al. Switching the chirality of a ferroelectric vortex in designed nanostructures by a homogeneous electric field. *Phys. Rev. B* **96**, 134119 (2017).
28. Tikhonov, Y. et al. Controllable skyrmion chirality in ferroelectrics. *Sci. Rep.* **10**, 8657 (2020).
29. Van Lich, L. et al. Deterministic switching of polarization vortices in compositionally graded ferroelectrics using a mechanical field. *Phys. Rev. Appl.* **11**, 054001 (2019).
30. Chen, W. J. et al. Mechanical switching in ferroelectrics by shear stress and its implications on charged domain wall generation and vortex memory devices. *RSC Adv.* **8**, 4434–4444 (2018).
31. Ma, L. L. et al. Mechanical writing of in-plane ferroelectric vortices by tip-force and their coupled chirality. *J. Phys. Condens. Matter* **32**, 035402 (2019).
32. Geng, W. et al. Rhombohedral–orthorhombic ferroelectric morphotropic phase boundary associated with a polar vortex in BiFeO₃ films. *ACS Nano.* **12**, 11098–11105 (2018).
33. Vorotiahin, I. S. et al. Tuning the polar states of ferroelectric films via surface charges and flexoelectricity. *Acta Mater.* **137**, 85–92 (2017).
34. Morozovska, A. N. et al. Interfacial polarization and pyroelectricity in anti-ferrodistortive structures induced by a flexoelectric effect and rotostriction. *Phys. Rev. B* **85**, 094107 (2012).
35. Eliseev, E. et al. Flexo-elastic control factors of domain morphology in core-shell ferroelectric nanoparticles: soft and rigid shells. *Acta Mater.* **212**, 116889 (2021).
36. Morozovska, A. N. et al. Flexo-sensitive polarization vortices in thin ferroelectric films. *Phys. Rev. B* **104**, 085420 (2021).

37. Morozovska, A. N. et al. Introducing the flexon–a new chiral polarization state in ferroelectrics. *arXiv:2104.00598 [cond-mat.mtrl-sci]* (2021).

38. Li, Q. et al. Quantification of flexoelectricity in $PbTiO_3/SrTiO_3$ superlattice polar vortices using machine learning and phase-field modeling. *Nat. Commun.* **8**, 1468 (2017).

39. Wachowiak, A. et al. Direct observation of internal spin structure of magnetic vortex cores. *Science* **298**, 577–580 (2002).

40. Uhlíř, V. et al. Dynamic switching of the spin circulation in tapered magnetic nanodisks. *Nat. Nanotechnol.* **8**, 341–346 (2013).

41. Peng, R.-C. et al. Switching the chirality of a magnetic vortex deterministically with an electric field. *Mater. Res. Lett.* **6**, 669–675 (2018).

42. Baek, S. H. et al. Ferroelastic switching for nanoscale non-volatile magnetoelectric devices. *Nat. Mater.* **9**, 309–314 (2010).

43. Balke, N. et al. Deterministic control of ferroelastic switching in multiferroic materials. *Nat. Nanotechnol.* **4**, 868–875 (2009).

44. Mantri, S. et al. Domain walls in ferroelectrics. *J. Am. Ceram. Soc.* **104**, 1619–1632 (2021).

45. Fousek, J. et al. The orientation of domain walls in twinned ferroelectric crystals. *J. Appl. Phys.* **40**, 135–142 (1969).

46. Li, Q. et al. Giant elastic tunability in strained $BiFeO_3$ near an electrically induced phase transition. *Nat. Commun.* **6**, 8985 (2015).

47. Liu, D. et al. Phase-field simulations of surface charge-induced ferroelectric vortex. *J. Phys. D: Appl. Phys.* **54**, 405302 (2021).

48. Tian, Y. et al. Water printing of ferroelectric polarization. *Nat. Commun.* **9**, 3809 (2018).

49. Ma, J. et al. Acidic aqueous solution switching of magnetism in $BiFeO_3/La_{1-x}Sr_xMnO_3$ heterostructures. *J. Appl. Phys.* **126**, 075301 (2019).

50. Cao, Y. et al. Electronic switching by metastable polarization states in $BiFeO_3$ thin films. *Phys. Rev. Mater.* **2**, 094401 (2018).

51. Chen, L.-Q. Phase-field method of phase transitions/domain structures in ferroelectric thin films: a review. *J. Am. Ceram. Soc.* **91**, 1835–1844 (2008).

52. Li, Y. L. et al. Phase-field model of domain structures in ferroelectric thin films. *Appl. Phys. Lett.* **78**, 3878–3880 (2001).

53. Wang, J. et al. Phase-field simulations of ferroelectric/ferroelastic polarization switching. *Acta Mater.* **52**, 749–764 (2004).

54. Vasudevan, R. K. et al. Domain wall geometry controls conduction in ferroelectrics. *Nano Lett.* **12**, 5524–5531 (2012).

55. Peng, R.-C. et al. Domain patterns and super-elasticity of freestanding $BiFeO_3$ membranes via phase-field simulations. *Acta Mater.* **208**, 116689 (2021).

56. Zheng, Y. et al. Thermodynamic modeling of critical properties of ferroelectric superlattices in nano-scale. *Appl. Phys. A* **97**, 617 (2009).

57. Rupprecht, G. et al. Dielectric constant in paraelectric perovskites. *J. Phys. Rev.* **135**, 748–752 (1964).

58. Liu, D. et al. Phase-field simulations of surface charge-induced polarization switching. *Appl. Phys. Lett.* **114**, 112903 (2019).

ACKNOWLEDGEMENTS

AUTHOR CONTRIBUTIONS

D.L. and H.B.H. contributed to the design of this study, in the acquisition and interpretation of the supporting data, and in the drafting of the text. J.W., H.M.J. and X.Y.W. contributed to the writing and data interpretation. C.Y., X.M.S., D.S.L. and X.W.C. provided many valuable discussions.

COMPETING INTERESTS

The authors declare no competing interests.

ADDITIONAL INFORMATION

Supplementary information The online version contains supplementary material available at https://doi.org/10.1038/s41535-022-00444-8.

Correspondence and requests for materials should be addressed to Houbing Huang.

Reprints and permission information is available at http://www.nature.com/reprints

Publisher's note Springer Nature remains neutral with regard to jurisdictional claims in published maps and institutional affiliations.